

Automatic Detection of Sub-Kilometer Craters in High Resolution Planetary Images

Erik R. Urbach^a, Tomasz F. Stepinski^a

^aLunar and Planetary Institute, Houston TX 77058, USA

Abstract

Impact craters are among the most studied geomorphic planetary features because they yield information about the past geological processes and provide a tool for measuring relative ages of observed geologic formations. Surveying impact craters is an important task which traditionally has been achieved by means of visual inspection of images. The sheer number of smaller craters present in high resolution images makes visual counting of such craters impractical. In this paper we present a method that brings together a novel, efficient crater identification algorithm with a data processing pipeline; together they enable a fully automatic detection of sub-km craters in large panchromatic images. The technical details of the method are described and its performance is evaluated using a large, 12.5 m/pixel image centered on the Nanedi Valles on Mars. The detection percentage of the method is ~70%. The system detects over 35,000 craters in this image; average crater density is 0.5 craters/km², but localized spots of much higher crater density are present. The method is designed to produce “million craters” global catalogs of sub-km craters on Mars and other planets wherever high resolution images are available. Such catalogs could be utilized for deriving high spatial resolution and high temporal precision stratigraphy on regional or even planetary scale.

Key words: Crater detection algorithms, crater counting, stratigraphy, Mars

1. Introduction

Impact craters are structures formed by collisions of meteoroids with the planetary surface. The importance of impact craters stems from the wealth of information that detailed analysis of their distributions and morphology can bring forth. For example, statistics of crater sizes form the basis for geological stratigraphy of the Moon and Mars [8, 29, 23]. Crater counts are the only available tool for measuring remotely the relative ages of geologic formations on planets. In addition, knowledge of crater morphologies enables studies of a number of outstanding issues in planetary geomorphology, such as: the nature of degradational processes [20], regional variations in geologic material [6], and distribution of subsurface volatiles [7]. Thus, surveying impact craters is an important task in planetary research. Presently, all such surveys are done manually. For example, the most comprehensive catalogs of craters on Mars contain information on 42,283 craters [4], and 57,633 craters [16], respectively. They contain only craters larger than 5 km in diameter. For the Moon the most comprehensive catalog [1] lists 8,497 named craters that are larger than few kilometers in diameter. For Mercury and the icy satellites of outer planets much less extensive catalogs of large craters have been compiled. No comprehensive catalogs of smaller, sub-km craters exist for any planetary body. This is because building such a data set is a very laborious process, ill-suited for visual detection but well-suited for an automated technique.

Automating the process of crater detection is the only practical solution for comprehensive surveys of smaller craters. Such surveys can deliver regional or even global coverage making million craters catalogs a reality and facilitating an objective

and repeatable analysis, well beyond and above of what can be analyzed using manually processed data sets.

Auto-detection of craters in planetary images is not a new idea; Salamuniccar and Loncaric [17] have tabulated 73 publications devoted to various techniques of crater detection. We refer to their tabulation for a complete record of previous work on crater detection algorithms. Despite this large body of work, practitioners of planetary science continue to count craters manually, and we are not aware of any applications of crater detection algorithms to actual planetary research. This is because the early approaches to crater detection were not developed beyond a demonstration stage and were not demonstrated to be robust to changes in a character of planetary surface thus limiting their appeal in actual applications. Only the most recent crater detection algorithms, that borrow techniques from the field of face detection, appear to be robust enough for practical applications. Kim et al. [12] use combination of edge detection, template matching, and neural network-based scheme for recognition of false positives to construct a system for auto-detecting craters on Mars. In a different approach, Martinez et al. [13] adopted a boosting algorithm, originally developed by Viola and Jones [27] in the context of face detection, for identification of craters on Mars. Although these new approaches show high detection accuracy, the underlying technology is complicated and its robustness to different terrain types and to image quality were not demonstrated.

In this paper we present a different approach to auto-detection of craters in panchromatic planetary images. The key insight behind our method is an observation that a crater can be recognized in an image as a pair of crescent-like highlight and shadow regions. Therefore, our method utilizes mathematical

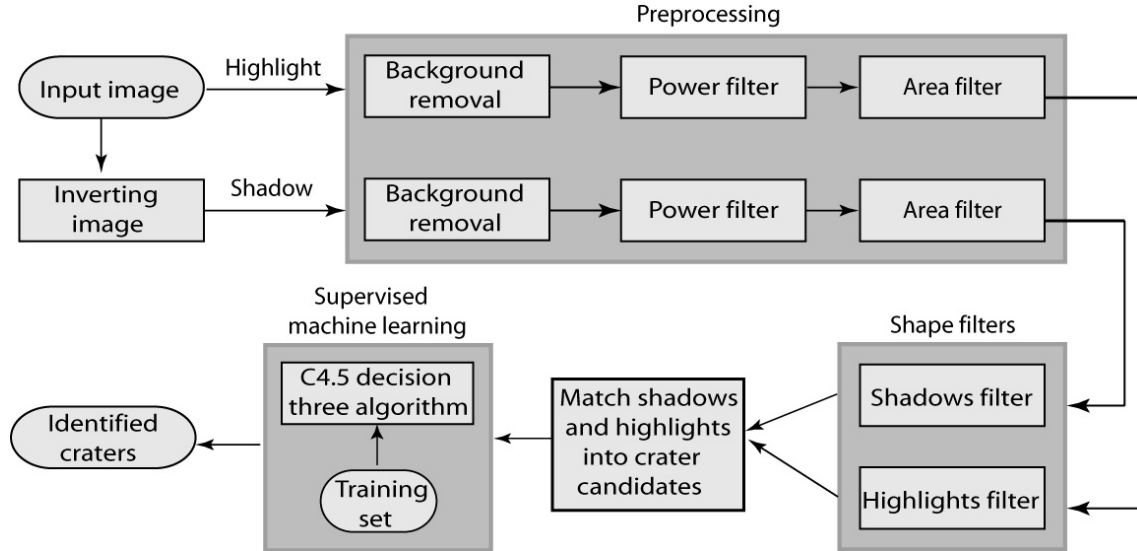


Figure 1: Diagram illustrating consecutive steps in mathematical morphology-based algorithm for identification of craters.

morphology [14, 18] for the task of crater detection; scale and rotation-invariant shape filters are used to identify crescent-like regions in an image. Subsequently, we utilize supervised machine learning techniques to distinguish between regions that are craters and those which are not. This approach, based on a relatively simple principle, promises to be robust and efficient, making it well-suited for large-scale, regional or global surveys of small craters. Our focus is on surveys of sub-km craters because larger craters can be identified either manually [4, 16], or using a topography-based algorithm [21, 22]. The present paper describes the core crater detection algorithm based on principle of mathematical morphology, gives the assessment of its performance, and shows how it can be utilized for large scale surveys of craters.

The rest of the paper is organized as follows. Section 2 describes the core crater identification algorithm. In Section 3 we present the results of applying our method to a very large, 12.5 meters/pixel panchromatic image of Mars taken by the High Resolution Stereo Camera (HRSC) instrument on-board the Mars Express spacecraft; both accuracy assessment and full image crater survey are presented. Conclusions and future research directions are given in Section 4.

2. Methods

Fig. 1 shows a diagram illustrating individual steps in our core algorithm. The input is a panchromatic image which contains many highlight and shadow features. The algorithm processes highlight and shadow features in parallel using inverted image to process the shadow features. The goal of the chain of processes is to eliminate all features that are not indicative of craters. The remaining highlight and shadow features are matched to each other to flag regions that are candidates for being craters. In the final step a supervised machine learning

technique is used to distinguish between true craters and non-crater regions. The feature processing pipeline uses extensively the attribute filters [5] including power filter, area filter, and shape filter. An attribute filter uses a criterion evaluated using attributes of image features to decide whether to remove or keep unchanged any given feature. For example, if an attribute is the number of pixels contained in a feature and the criterion is “attribute value $> \lambda$ ”, then a corresponding attribute filter removes all image features that contain less than λ pixels. The attributes used in our method are invariant to translation and rotation, which means that corresponding attribute filters remove all image features that do not satisfy the criterion regardless of the position and orientation of each feature. The shape attributes used are also scale invariant. Thus, a single application of an attribute filter to an image removes all undesired features thereby saving computational cost in the processing pipeline.

2.1. Preprocessing

An image of planetary surface contains many highlight and shadow features that are either not parts of craters or are parts of large craters that are of no interest to our present method. Thus, in the preprocessing step, we apply a series of filters to remove such features.

- **Background removal:** This step removes background features such as mountains that are too large to be part of the craters. A median filter is applied to the input image, resulting in an image containing only the global features of the background; by subtracting this median-filtered image from the input image, a new image is obtained which no longer contains the large background features. A median filter used in test sites uses a 201 pixels wide circular window.
- **Power filter:** The power filter [30] removes features that are (almost) invisible: they are too small and/or they lack

sufficient contrast to be noticed by humans and can therefore also not be used for reliable processing. We implement the power filter as an attribute filter with the power attribute defined as $P = A(h_a - h_b)^2$ using variables computed from an image feature: its area A , its gray-level h_a and the gray-level h_b of the darkest neighboring feature that is still brighter than h_a . Features with $P < P_0$ are removed. We use $P_0 = 1000$ in test calculations.

- **Area filter:** The area filter is an attribute filter using the number of pixels in a feature as its attribute. This filter removes all features that are considered too small for reliable crater detection. Features with $A < A_0$ are removed. We use $A_0 = 30$ in test calculations.

2.2. Shape filters

After removal of features that are either too large, too small, or lack sufficient contrast, the next step in our method is to remove features that have shapes irreconcilable with craters. For this purpose we employ a shape filter that uses a shape attribute. In order to achieve a sufficient level of discrimination between crater and non-crater features, the shape attribute is a vector containing Hu’s seven moment invariants [9]. These invariants are easy to implement and efficient to compute [24]. So-defined shape attribute is invariant to translation, rotation, and scaling [25]; the corresponding shape filter preserves or removes image features based exclusively on their shapes without regard to their size, orientation or location. Thus, only one pass over all features is needed to remove all the features whose shape does not satisfy the given criterion.

Shape rejection criterion is based on the minimum Euclidean distance between a shape attribute of a feature and a set of shape attributes belonging to a library of reference shapes chosen to represent characteristic highlight and shadow regions of the craters. In test calculations the number of reference shapes for the highlights and shadow regions was 17 and 12, respectively. An image feature having distance of less than 0.05 to at least one of the reference shapes is preserved for further processing.

2.3. Matching highlight and shadow regions

Preprocessing and application of shape filters yield two images: one containing highlight regions that are likely to be the parts of craters and another containing shadow regions that are likely to be the complementing parts of craters. The next step in our method is to match highlight regions to shadow regions so each pair corresponds to a single crater. This step is important because it incorporates additional knowledge into final crater identification. As each crater must appear as a pair of highlight and shadow regions with proper sizes, shapes, and relative locations, regions that cannot be matched are not considered to correspond to craters. To obtain crater candidates we match the highlight and shadow regions using simple rules. Regions that cannot be matched are discarded. Each possible pair of highlight (H) and shadow (S) regions are considered. A pair (H, S) must satisfy all of the following rules to be considered a crater candidate:

1. Distance between H and S must be smaller than a threshold proportional to the regions size. This removes pairs of H and S regions that are too far away from each other. We use $1.65\sqrt{A_H}$ as the threshold, where A_H is the area of H.
2. The regions H and S should have similar sizes. In present calculation the difference in size cannot be larger than 4.
3. The elongation of combined H and S regions must be smaller than a threshold; only pairs with a round combined shape are preserved. The measure of elongation is provided by the first of Hu’s seven moments invariants. We reject pairs with combined shape having the first moment invariant larger than 3.
4. The elongation of combined H and S regions must be less than individual elongations of H and S.
5. The H and S regions must align along the orientation dictated by a solar illumination angle.

2.4. Supervised classification

The above rules have been established experimentally and they provide a “first cut” list of crater candidates. For further refinement of that list we use supervised classification. First, the shape and size of each candidate is estimated by filling the space between its constituent H and S regions using a morphological closing operation with an ellipse as the structuring element. Each candidate is assigned a multidimensional vector of attributes which consists of Hu’s seven moments invariants computed for the approximate shape of the candidate and the variables computed in the process of executing the rules enumerated in section 2.3. We discriminate between craters and non-craters among the candidates using the technique of supervised classification. A supervised learning uses a training set of crater candidates, for which crater or non-crater labels have been already assigned manually by an analyst. This training set is utilized by a learning algorithm to construct a labeling function (a classifier) that is then applied to label all other crater candidates. Such classifier is an extensive, computer-derived set of rules that reflects a connection between candidates numerical features and their labels. In this paper a classifier is constructed using the C4.5 decision tree technique [15]. Applying the resultant classifier to the list of crater candidates yield the final catalog of identified craters.

3. Results

3.1. Test site

We have selected the HRSC nadir panchromatic image h0905_0000 to serve as a test site. This large (8248×65448 pixels) image represents a significant challenge to automatic crater detection because of its size and uneven illumination. The site is located between longitudes of $-47^\circ.22\text{E}$ and $-49^\circ.0\text{E}$, and the latitudes of $0^\circ.3\text{S}$ and $-18^\circ.48\text{N}$. Fig. 2 shows the geographical and geologic context of the test site; the site is located in the Xanthe Terra, centered on Nanedi Valles and covers mostly Noachian terrain. With image resolution being 12.5 m/pixel, site’s north-south extension is 818 km and its east-west extension is 103 km.

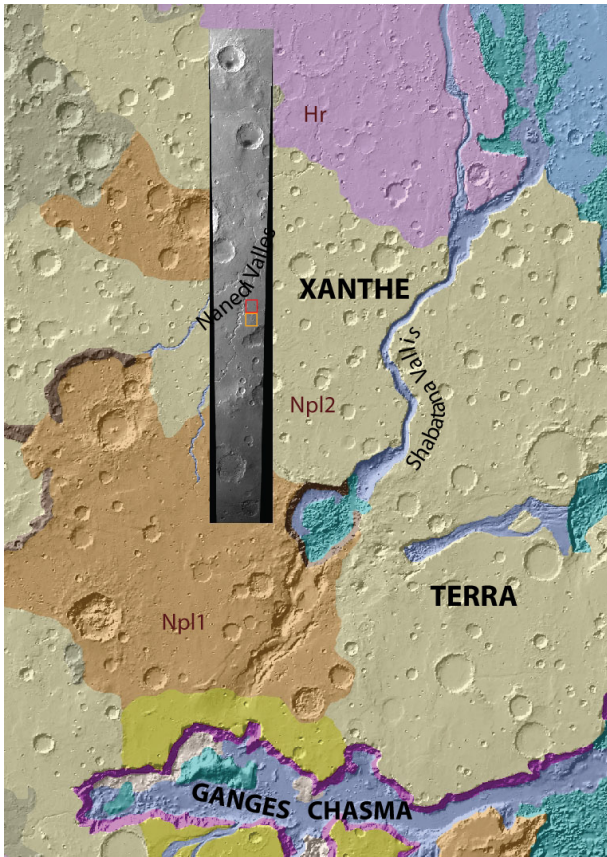


Figure 2: Geographical and geologic context of the test site. The HRSC image h0905_0000 is overlaid on a map showing regional topography and geological units. The location of the training tile is indicated by a red rectangle, and the location of the test tile is indicated by an orange rectangle.

A file containing the h0905_0000 image has a size of 515 Mb. Because of memory considerations, a crater detection algorithm cannot process the entire image at once while running on a typical PC computer. We have developed a processing pipeline for surveying craters in high resolution images (like the h0905_0000 image) having very large file size. First, we tessellate the entire image with overlapping tiles, so each tile, having relatively small size, can be processed separately. The tiles overlap to ensure detection of craters located on the boundaries of the tiles. The h0905_0000 image was tessellated into $44 \times 6 = 264$ tiles, each containing 1700×1700 pixels. Neighboring tiles have a 200 pixel overlap. Craters are detected from each tile and a local catalog of craters identified within a tile is created. By combining all tile-specific catalogs, a complete catalog for the entire image is created. Finally, duplicate craters resulting from tiles overlapping are eliminated.

3.2. Training and testing tiles

Before applying our crater detection algorithm to the entire h0905_0000 image we first apply it to a couple of single tiles having dimensions of 1700×1700 pixels each. We have chosen a tile labeled 3_24 as a “training site” and a tile labeled 3_25 as a “testing site.” The tile label reflects horizontal and vertical

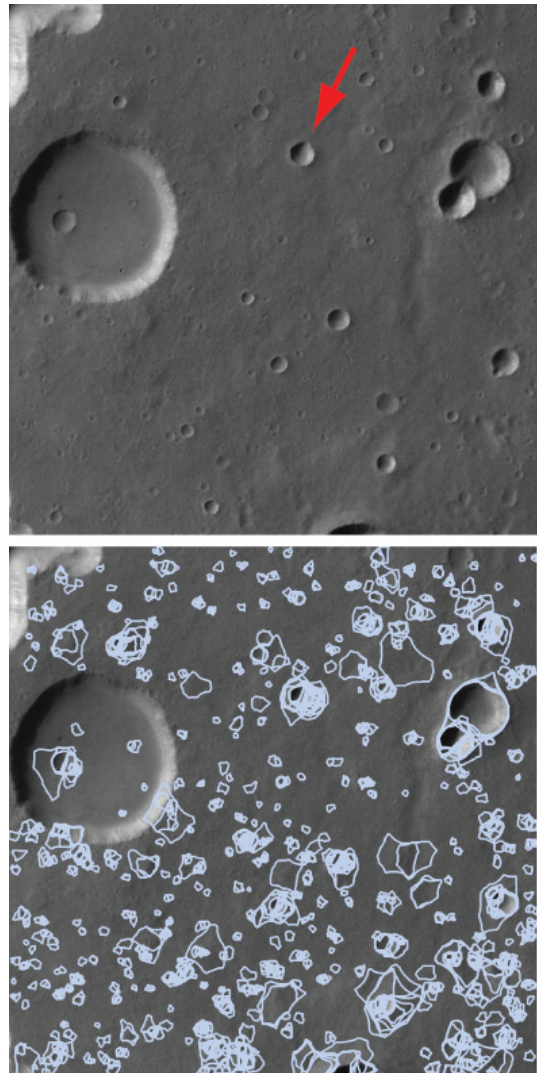


Figure 3: (Top) A panchromatic, 12.5 m/pixel resolution image of the tile 3_24; the red arrow points toward a 1 km size crater to give a sense of scale. (Bottom) Crater candidate shapes are shown in blue overlaid on an image of tile 3_24.

locations of the tile in a tessellated image. The location of the training tile is shown by the red rectangle on Fig. 2, and the location of the testing site is shown by the orange rectangle. The training site is used to manually label characteristic examples of crater and non-crater image features. The testing site is used to evaluate the performance of a classifier on an image that is not contributing any features to the training set.

The upper part of Fig. 3 shows an image of the 3_24 tile. The red arrow indicates a 1-km-size crater to give a sense of scale. Great majority of craters within the tile are sub-km craters. The lower part of Fig. 3 shows 1543 crater candidates identified by our algorithm using shape filters, but before applying a supervised classification. It is clear that shape filters alone are not sufficient to identify the craters; they allow many false positive detections.

In order to apply a supervised classification we need to establish a training set, a collection of crater candidate shapes that

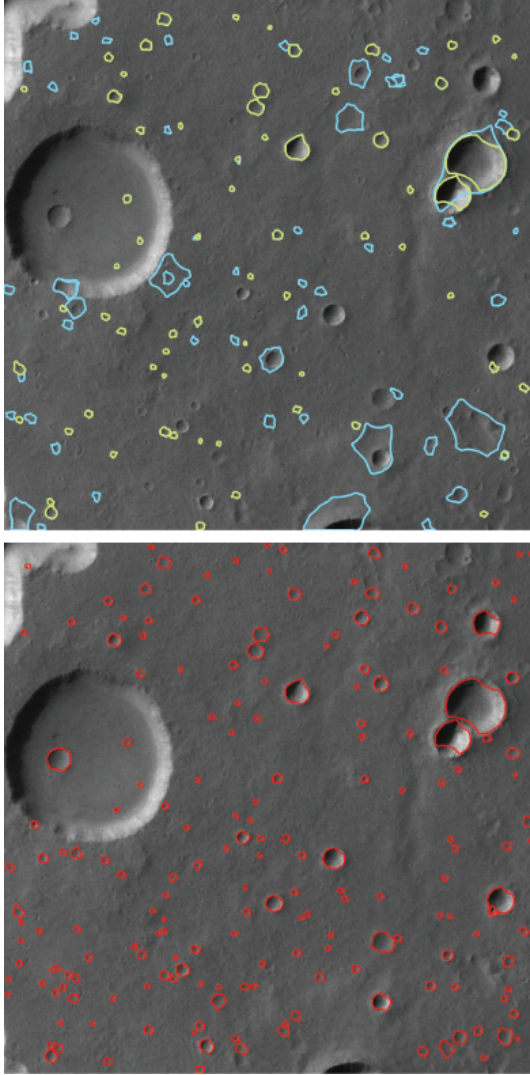


Figure 4: (Top) Training shapes: yellow outlines indicate craters, blue outlines indicate non-crater feature. (Bottom) Craters detected by our algorithm are indicated by red outlines. Note that the largest crater in the image is not identified because it exceeds the 5 km size limit.

are labeled by an expert to be either craters or non-craters. From among the 1543 crater candidates identified in the 3_24 tile, we have marked selected 69 shapes that are indeed craters. These positive examples are shown as yellow outlines on Fig. 4. We have also marked 59 features that are in the group of crater candidates but are not craters; these are shown as blue outlines on Fig. 4. The positives and negatives examples are used to train the C4.5 classifier. The resultant classifier was applied to all 1543 candidates resulting in marking 185 of them as craters and the rest as non-craters. The identified craters are shown as red outlines in Fig. 4.

In the test site the algorithm finds 2112 crater candidates. The supervised classifier (trained on the training site) labels 234 of them as craters and the rest as non-crater features.

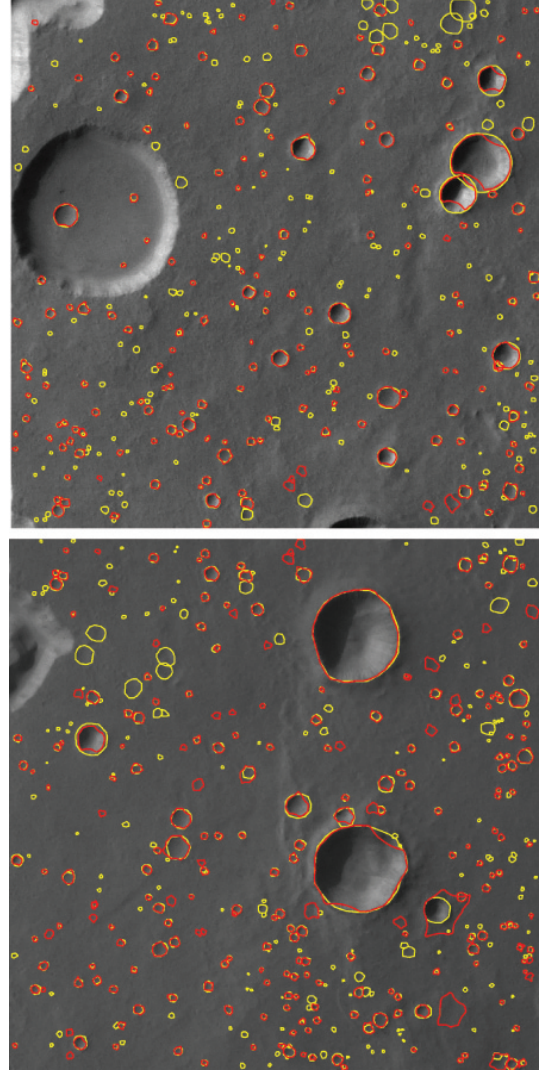


Figure 5: Comparison of craters detected by our algorithm (red) and manually marked by an analyst (yellow). (Top) Training site, tile 3_24. (Bottom) Test site, tile 3_25.

3.3. Testing performance of crater auto-detection algorithm

The performance of our algorithm is evaluated using training and testing tiles. Craters in both sites were manually marked to provide ground truth used for quality assessment. The ground truth data contains 351 craters in the training site and 360 craters in the test site. Fig. 5 shows craters marked by an analyst and craters detected by our algorithm in training and test sites, respectively. Table 1 lists the crater counts in the both sites. The table is divided into two categories: all craters and the craters larger than 200 meters in diameter. Because our method is designed to detect craters larger than ~ 20 pixels in diameter, we expect only craters larger than ~ 200 meters to be systematically detected in HRSC images. However, an analyst has marked all craters visible to a human eye, many of them smaller than 200 m in diameter. The fair comparison is between algorithmically detected craters and manually detected craters larger than 200 m in diameter.

| | TP | FP | FN |
|---------------------------------|-----|----|-----|
| Training site (all) | 175 | 10 | 176 |
| Training site ($D \geq 200m$) | 109 | 8 | 45 |
| Test site (all) | 198 | 36 | 162 |
| Test site ($D \geq 200m$) | 120 | 35 | 57 |

Table 1: Crater counts.

| | D | B | Q |
|---------------------------------|-------|------|-------|
| Training site (all) | 49.9% | 0.06 | 48.5% |
| Training site ($D \geq 200m$) | 70.8% | 0.09 | 66.5% |
| Test site (all) | 55% | 0.18 | 50% |
| Test site ($D \geq 200m$) | 67.8% | 0.29 | 56.6% |

Table 2: Quality of crater detection.

We use quality factors developed in [19]: detection percentage $D = 100TP/(TP + FN)$, branching factor $B = FP/TP$, and quality percentage $Q = 100TP/(TP + FP + FN)$, to assess the performance of our algorithm. Here, TP stands for the number of true positive detections (identified craters that are actual craters), FP stands for the number of false positive detections (incorrectly identified craters that are not actual craters), and FN stands for the number of false negative detections (non-detection of real craters). D can be treated as a measure of crater-detection performance, B can be treated as a measure of delineation performance, and Q can be treated as an overall measure of algorithm performance.

Table 2 lists the quality factors resulting from comparing craters detected by our algorithm to the manually identified craters. This table is again divided into two categories, all crater and the craters larger than 200 m in diameter. As expected the results are better if only craters with diameters > 200 m are taken into account. This is because smaller craters lack sufficient number of pixels for reliable machine identification. Interestingly, the performance on both sites is about the same indicating that the limited set of examples established in the training site are equally representative for both sites.

Overall, the performance of our algorithm is $D \sim 70\%$ and $Q \sim 55 - 65\%$. The most direct performance comparison can be made with an algorithm developed by [12] which was also tested using HRSC panchromatic, 12.5 m/pixel resolution images. They reported $D \sim 70\%$ and $Q \sim 62\%$ when tested on small craters in the Olympus Mons part of the h037_0000 image. Performance of $D \sim 86\%$ and $Q \sim 73\%$ was reported in [3] using an algorithm based on template matching. However, they tested their algorithm only on images taken by the Mars Orbiter Camera (MOC) in its wide-angle mode and having resolution of 200-300 m/pixel. In addition, they applied their algorithm exclusively to sites located in the Hesperian terrain. In [13] the same images were used to assess a performance of a crater detection algorithm based on a boosting approach and even slightly better performance was reported. The high performance reported by [3, 13] may be attributed to the fact that large craters in a Hesperian terrain are very regular and relatively easy to identify. It is unknown how these algorithms would perform when applied for detection of small craters in more challenging surfaces.

3.4. Surveying sub-km craters in the entire h0905_0000 image

For the survey of craters in the entire h0905_0000 image we have used expanded training set constructed using the tiles: 1_23, 2_25, 3_23, 3_24, and 4_25. The total number of training examples is 2611, with 1994 examples of characteristic crater

shapes and 617 examples of characteristic non-crater shapes. We have embedded our crater identification algorithm into a data processing pipeline; without this pipeline it would take a significant time and effort to process each of the 264 tiles separately. The processing pipeline employs scripts that automate the entire process. The supervised classifier is run using Java-based routines, components of the WEKA [28] environment. The pipeline produces the final catalog of craters and also a set of ArcGIS [2] project files, each pertaining to a single tile. An ArcGIS project contains all the information about the single tile in the GIS format including the tile image, crater candidates, detected craters, etc. These project files are valuable byproducts of a survey. For example, in some studies it may be crucial to count craters as accurately as possible in a relatively small region. In such a case, an ArcGIS project file covering this region can be used to manually correct an automatic survey. On the other hand, an auto-survey offers a ‘‘carpet coverage’’ of sub-km craters over the large regions of the planet. The accuracy of such a survey may not be on par with the accuracy of manual mapping, but it is sufficient for statistical purposes and much more practical.

Fig. 6 shows locations of the 35,495 craters identified by our process in the h0905_0000 image. For such a massive survey a validation process as described in the previous subsection is not feasible. However, visual inspection of an image with the locations of the craters superimposed on it indicates performance on par with that reported for tiles 3_24 and 3_25.

The craters identified by the auto-survey span the sizes from 112 m to 6 km. The size-frequency distribution (SFD) of all the craters identified in an image is shown on Fig. 7. It is clear from the observed fall off in the number of craters having diameters smaller than ~ 200 m that our algorithm has a detectability threshold of ~ 200 m or about 10-20 pixels. There is also a smaller fall off at the upper threshold of detectability. This upper threshold is artificially introduced to reduce computational time of the survey and can be adjusted. The comparison of the SFD constructed from detected craters with isochrons proposed by [10, 11] indicates the age (Noachian) of the underlying surface in agreement with the age inferred from counting larger craters [23].

The most striking result coming out of the survey is an uneven, patchy character of spatial distribution of craters. Fig. 6 shows a map of the local crater density as calculated using a moving window technique with the size of 100 pixels. This map shows that although an average crater density is 0.5 craters/km², local ‘‘hot spots’’ with twice that density are present. The largest crater-enhancement spot is located just to the west of a large, 43-km-size, crater centered at $-47^{\circ}.86E$ and $10^{\circ}.49N$.

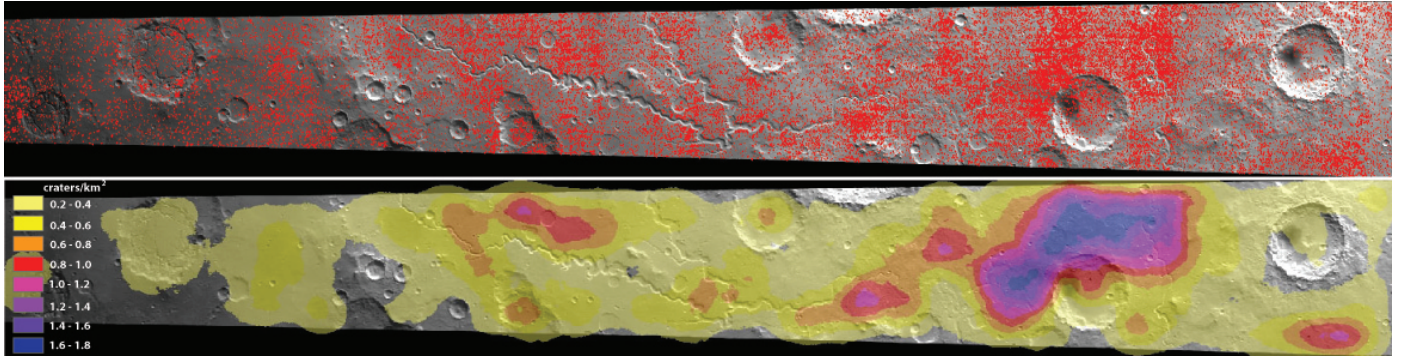


Figure 6: Auto-survey of sub-km craters in the HRSC image h0905_0000. (Top) Crater centers are indicated by red dots overlaid on the image. (Bottom) Local crater density. In both panels the north direction is to the right.

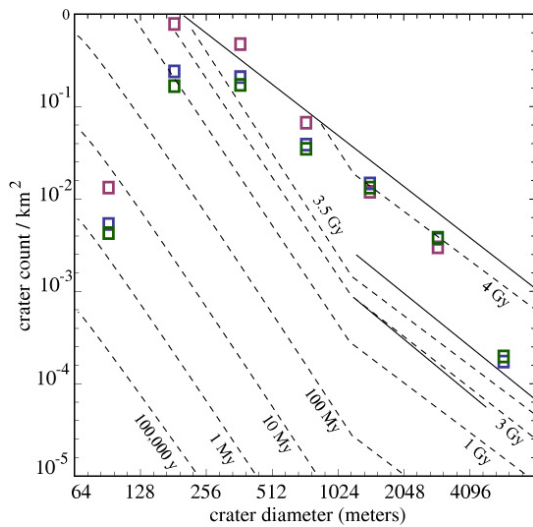


Figure 7: Size-frequency distribution for craters identified in the HRSC image h0905_0000. The blue marks indicate counts using all craters in an image, the red marks indicate counts using only craters located within the crater-enhanced spots, and the green marks indicate counts using only craters located outside the crater-enhanced spots. Dotted lines represent isochrones, the upper solid line marks saturation equilibrium, and the other solid lines mark divisions of Amazonian, Hesperian, and Noachian eras.

The crater density in the middle of this spot approaches 2 craters/km². The presence of these spots is not an artifact of the detection method. Visual inspection confirms existence of many more real craters in these regions.

In order to study further these spots, we have constructed an inclusive mask containing these parts of the image where crater density exceeds 0.8 craters/km². On Fig. 6 these are areas shown in red or darker colors. The masked region constitutes only 12% of site's area, but it contains 11,362 or 32% of all the craters. The SFD of the craters located within the masked area is also shown on Fig. 7. The distribution is steeper than that constructed from all the craters in the site indicating relatively more small craters. We have also derived the SFD for the 24,133 craters located outside the masked region. The SFDs constructed for these craters is not noticeably different from the

SFD constructed for all the craters. Thus, within the spots small craters are even more dominant than is expected. Explaining the origin of these spots is beyond the scope of the present paper; these may be regions where secondary craters are concentrated, but no clear pattern of the spots is observed with the constraints of the image h0905_0000.

4. Conclusions

In this paper we have presented a novel approach to detecting craters in planetary images. This approach minimizes computation time while achieving accuracy comparable to other recently published crater detection algorithms. On the h0905_0000 footprint used ($8248 \times 65448 = 539,815,104$ pixels) 14 hours of computing time were needed, which can be divided into 7 hours for tiling, preprocessing, and the shapefilters, 6.3 hours for the supervised machine learning, and 0.6 hours for removing doubles. The total computing time equals to an average processing speed of 10,710 pixels per second or 93 microseconds per pixel. Because of its features we propose that our algorithm is a viable tool for comprehensive, large-scale auto-surveys of sub-km craters in high resolution planetary images. The paper brings together a new core crater detection algorithm based on mathematical morphology methods with a data processing pipeline that allows fully automatic survey of craters in a very large image.

At present an accuracy of our algorithm, as measured by the detection percentage, is about 70% for sub-km craters on the Noachian terrain. Although we did not test the performance of our algorithm on larger craters and/or other types of surfaces, it is expected that small craters on Noachian surface presents the toughest challenge to auto-detection.

Future versions of our algorithm will show an improved performance. This can be achieved by a number of revisions. First, a decision to reject or retain a shape (see section 2.2) could be based on a machine learning instead of comparison to a limited number (29) of arbitrarily chosen shapes. Second, the matching criteria (see section 2.3) could be reviewed and potentially replaced completely by a decision function generated by a supervised classifier that uses a large training set. This means

combining steps described in sections 2.3 and 2.4. Finally, the present algorithm uses supervised classifier based on the C4.5 method; other classification methods, such as, for example, the Support Vector Machine [26] should be tested and may offer improved performance.

Our method can be used to expedite crater counting in order to establish relative and absolute chronologies of planetary surfaces. Typically, craters with diameters > 1 km are used for such purpose because manual counting becomes exceedingly tedious with decreasing crater size. However, only relatively large regions can be dated by counting craters having size > 1 km because sufficient number of craters must be accumulated to reduce uncertainties associated with statistical comparison of counts. In order to resolve various ages of smaller regions, counts of sub-km craters, which are orders of magnitude more frequent, are needed. Because counts of sub-km craters have lower statistical uncertainties, they can be used to recognize smaller differences in age, or smaller areas of different age. Our auto-detection method, that delivers means of compiling a “million craters” catalog of sub-km craters, can, in principle, be utilized to produce high resolution and high precision global stratigraphy.

Spatially extensive surveys of small craters may produce surprises and lead to new discoveries. For example, our survey of the HRSC image h0905_0000 reveals patchy distribution of craters and existence of prominent spots of enhanced crater density in an area that otherwise appear to be uniform in age and geology. Surveying even larger regions of Mars may reveal other patterns in spatial distribution of sub-km craters.

Finally, our method is pixel-based and thus independent of a source and resolution of an image. In this paper we used an image of Mars taken by the HRSC instrument, but our algorithm can identify craters in any planetary image.

Acknowledgments. This work was supported by NASA under grant NNG06GE57G. The research was conducted at the Lunar and Planetary Institute, which is operated by the USRA under contract CAN-NCC5-679 with NASA. This is LPI Contribution No. ***.

References

- [1] Andersson, L. B., Whitaker, B. A., 1982. Nasa catalogue of lunar nomenclature. In: NASA Reference Publication 1097.
- [2] ArcGISWebPage, 2008. <http://www.esri.com>.
- [3] Bandeira, L., Saraiva, J., Pina, P., 2007. Impact crater recognition on mars based on a probability volume created by template matching. *IEEE Transactions on Geoscience and Remote Sensing* 45 (12), 4008–4015.
- [4] Barlow, N. G., 1988. Crater size-distributions and a revised martian relative chronology. *Icarus* 75 (2), 285305.
- [5] Breen, E. J., Jones, R., 1996. Attribute openings, thinnings and granulometries. *Comp. Vis. Image Understand.* 64, 604–614.
- [6] Cintala, M. J., Head, J., Mutch, T. A., 1976. Martian crater depth/diameter relationship: Comparison with the moon and mercury. *Proc. Lunar Sci. Conf.* 7, 33753587.
- [7] Cintala, M. J., Mouginiis-Mark, P. J., 1980. Martian fresh crater depth: More evidence for subsurface volatiles. *Geophys. Res. Lett.* 7 (5), 329332.
- [8] CraterAnalysisWorkingGroup, 1979. Standard techniques for presentation and analysis of crater size-frequency data. *Icarus* 37, 467474.
- [9] Gonzalez, R. C., E.Woods, R., 2002. *Digital Image Processing*, 2nd Edition. Addison-Wesley.
- [10] Hartmann, W. K., 1999. Martian cratering vi. crater count isochrons and evidence for recent volcanism from mars global surveyor. *Meteor. Planet. Sci.* 34, 167–177.
- [11] Hartmann, W. K., Neukum, G., 2001. Cratering chronology and evolution of mars. In: Altwegg, K., Ehrenfreund, P., Geiss, J., Huebner, W. F. (Eds.), *Composition and Origin of Cometary Materials*. Kluwer Academic Publishers, The Netherlands, pp. 165–194.
- [12] Kim, J. R., Muller, J.-P., van Gasselt, S., Morley, J. G., Neukum, G., 2005. Automated crater detection, a new tool for mars cartography and chronology. *Photogramm. Eng. Remote Sens.* 71 (10), 12051217.
- [13] Martins, R., Pina, P., Marques, J. S., Silveira, M., 2008. Crater detection by a boosting approach. *IEEE Geoscience and Remote Sensing Letters* accepted.
- [14] Matheron, G., 1975. *Random Sets and Integral Geometry*. John Wiley.
- [15] Quinlan, J. R., 1993. *C4.5: Programs for Machine Learning*. Morgan Kaufmann Publishers Inc., San Francisco, CA.
- [16] Salamuniccar, G., Loncaric, S., 2008. Gt-57633 catalogue of martian impact craters developed for evaluation of crater detection algorithms. *Planetary and Space Science* accepted.
- [17] Salamuniccar, G., Loncaric, S., 2008. Open framework for objective evaluation of crater detection algorithms with first test-field subsystem based on mola data. *Advances in Space Research* 42, 6–19.
- [18] Serra, J., 1982. *Image Analysis and Mathematical Morphology*, Volume 1. Academic Press, New York, 2 edition.
- [19] Shufelt, J. A., 1999. Performance evaluation and analysis of monocular building extraction from aerial imagery. *IEEE Trans. Pattern Anal. Mach. Intell.* 21 (4), 311326.
- [20] Soderblom, L. A., Condit, C. D., West, R. A., Herman, B. M., Kreidler, T. J., 1974. Martian planetwide crater distributions: Implications for geologic history and surface processes. *Icarus* 22 (3), 239263.
- [21] Stepinski, T. F., Mendenhall, M. P., Bue, B. D., 2007. Robust automated identification of martian impact craters. In: *Lunar and Planetary Science XXXVIII (CD-ROM)*. No. 1202. Lunar and Planetary Institute.
- [22] Stepinski, T. F., Urbach, E., 2008. Raster maps of craters depths in southern hemisphere of mars: Potential proxy for spatial distribution of ground ice. In: *Lunar and Planetary Science XXXIX (CD-ROM)*. No. 1272. Lunar and Planetary Institute.
- [23] Tanaka, K. L., 1986. The stratigraphy of mars. *J. Geophys. Res.* 91 (B13), 139158.
- [24] Urbach, E. R., Boersma, N. J., Wilkinson, M. H. F., 2005. Vector-attribute filters. in mathematical morphology. In: *40 Years On, Proc. Int. Symp. Math. Morphology (ISMM) 2005*. Paris, 18–20 April 2005, p. 95104.
- [25] Urbach, E. R., Roerdink, J. B. T. M., Wilkinson, M. H. F., 2007. Connected shape-size pattern spectra for rotation and scale-invariant classification of gray-scale images. *IEEE Trans. Pattern Anal. Mach. Intell.* 29 (2), 272285.
- [26] Vapnik, V., 1998. *Statistical Learning Theory*. Wiley-Interscience, New York.
- [27] Viola, P., Jones, M., 2004. Robust real-time face detection. *Inter. Journal of Computer Vision* 57 (2), 137–154.
- [28] WEKAWebPage, 2008. <http://www.cs.waikato.ac.nz/ml/weka/>.
- [29] Wise, D. U., Minkowski, G., 1980. Dating methodology of small, homogeneous crater populations applied to the tempe-utopia trough region on mars. In: *NASA Tech. Memo 81 776*. NASA Goddard Space Flight Center, Greenbelt, MD, p. 122124.
- [30] Young, N., Evans, A. N., 2003. Psychovisually tuned attribute operators for pre-processing digital video. *IEEE Proc. Vision, Image and Signal Processing* 150 (5), 277286.